Environmental Science Processes & Impacts

PAPER

View Article Online
View Journal | View Issue

Check for updates

Cite this: *Environ. Sci.: Processes Impacts*, 2025, **27**, 3903

Interplay of Fe and S biogeochemistry shapes *in situ* iron mineral transformations in contrasting intertidal sediments

L. Joëlle Kubeneck, †*[ad] Giulia Fantappiè,[a] Luiza Notini, [ae] Katherine A. Rothwell, [ab] Laurel K. ThomasArrigo [ac] and Ruben Kretzschmar [a]

The transformation and stability of iron (Fe) minerals in coastal sediments are closely linked to the sulfur (S) cycle, influencing the fate of nutrients, carbon, and contaminants. However, *in situ* studies of these interactions in coastal sediments remain limited. We investigated the transformation of lepidocrocite, goethite, and mackinawite in three intertidal field plots with contrasting Fe and S biogeochemistry. Fe minerals were enriched with ^{57}Fe and mixed with the sediment, allowing close contact with the other inorganic and organic components of the sediment. After 8 weeks, transformation products were assessed using ^{57}Fe Mössbauer spectroscopy. Regular porewater analysis complemented solid-phase analyses, supporting the understanding of transformation pathways and extents. Under low-sulfide, Fe-reducing conditions, lepidocrocite did not transform to more crystalline Fe-oxides such as goethite or magnetite. Instead, ~20% of the lepidocrocite transformed, mostly into a disordered Fe-phase, due to reductive dissolution and a small extent of sulfidation. Goethite, in contrast, remained apparently unchanged under the same conditions. These results indicate that both Fe-oxides may persist during extended anoxic periods under Fe-reducing conditions in coastal sediments and thus may influence elemental cycles. However, in sulfidic environments, lepidocrocite and goethite transformed into amorphous, nonstoichiometric Fe–sulfide and greigite. We hypothesize that amorphous Fe–sulfide precipitated first, later transforming into greigite; a potential precursor of pyrite formation. This is further supported by the transformation of synthetic mackinawite into greigite under high sulfide conditions, suggesting a sulfidation pathway that may eventually lead to pyrite formation in coastal sediments.

Received 18th March 2025
Accepted 7th October 2025

DOI: 10.1039/d5em00213c

rsc.li/espi

Open Access Article. Published on 18 2025. Downloaded on 14.05.2026 20:13:44.
This article is licensed under a Creative Commons Attribution 3.0 Unported Licence.

Environmental significance

Iron (Fe) mineral dynamics in coastal sediments are heavily influenced by the balance between dissolved Fe and sulfide. This balance determines whether Fe minerals transform into more stable Fe-oxide or Fe–sulfide phases. These transformations impact the sorption capacities of Fe minerals for nutrients, carbon, and contaminants, thereby affecting their cycling. In this study, we demonstrate that the *in situ* behavior of lepidocrocite, goethite, and mackinawite differs from previously reported laboratory and field studies in soils. Under low-sulfide, Fe-reducing conditions, Fe-oxides persisted with minimal reductive dissolution, whereas in sulfidic environments, Fe–sulfide minerals formed within 8 weeks. These findings enhance our understanding of Fe mineral dynamics in coastal ecosystems and are crucial for predicting the biogeochemical cycling of associated elements like nutrients and contaminants.

Introduction

Iron (oxyhydr)oxides (hereafter referred to as Fe-oxides) formed during weathering under oxic conditions are eventually transported to the oceans.[1,2] Before reaching the ocean, Fe-oxides can become trapped in sediments of coastal wetlands, such as salt marshes and intertidal flats. Additionally, Fe-oxides may form *in situ* within these wetlands due to ongoing redox cycling. Compared to deep ocean marine sediments, coastal sediments are often enriched in Fe-oxides.[2] These Fe-oxides play a crucial role in the biogeochemical cycling of contaminants and nutrients due to their ability to sorb these compounds and influence their chemical speciation.[3,4] However, as coastal sediments are

[a]*Soil Chemistry Group, Institute of Biogeochemistry and Pollutant Dynamics, Department of Environmental Systems Science, ETH Zürich, Universitätstrasse 16, CHN, Zürich, CH-8092, Switzerland. E-mail: joelle.kubeneck@ru.nl*

[b]*Biological and Environmental Sciences, University of Stirling, Stirling, FK9 4LA, United Kingdom*

[c]*Environmental Chemistry, University of Neuchatel, Avenue de Bellevaux 51, Neuchatel, CH-2000, Switzerland*

[d]*Department of Microbiology, Radboud Institute for Biological and Environmental Sciences, Radboud University, 6525 AJ Nijmegen, The Netherlands*

[e]*Department of Civil, Construction, and Environmental Engineering, University of Delaware, Newark, Delaware 19716, USA*

† Current address: TNO Geological Survey of the Netherlands, PO Box 80015, 3508 TA Utrecht, The Netherlands.

Open Access Article. Published on 18 2025. Downloaded on 14.05.2026 20:13:44.
This article is licensed under a Creative Commons Attribution 3.0 Unported Licence.

increasingly influenced by sea level rise and expanding anoxic zones, the biogeochemical cycling of Fe-oxides in coastal sediments is prone to changes.[5]

Under reducing conditions, dissimilatory Fe(III) reduction can lead to the reductive dissolution of Fe-oxides and the subsequent release of Fe(II). This dissolved Fe(II) can interact with remaining meta-stable Fe-oxides, such as ferrihydrite and lepidocrocite, catalyzing their transformation into more crystalline Fe-minerals like goethite or magnetite.[6–8] In coastal environments, where sulfate reduction is a major pathway for organic matter mineralization,[9–11] the Fe and sulfur (S) cycles are closely linked.[11] Sulfate reduction produces dissolved sulfide, which interacts with Fe-oxides in various ways. For instance, sulfide oxidation coupled with Fe reduction can cause the reductive dissolution of Fe-oxides, releasing dissolved Fe(II) and forming oxidized sulfur species such as elemental sulfur and polysulfides.[12–14] The resupply of sulfate and production of polysulfides and/or intermediate S species can drive further redox reactions, resulting in a cryptic S cycle, as many S intermediates are not detectable in bulk measurements.[15,16] During these reactions, the dissolved Fe(II) can either catalyze Fe-oxide recrystallization and transformation or precipitate with dissolved sulfide as Fe–sulfide minerals.[17–20]

Fe-oxides such as ferrihydrite and lepidocrocite, which are thermodynamically meta-stable, undergo Fe(II)-catalyzed transformation or sulfide-promoted reductive dissolution within hours when exposed to dissolved Fe(II)[6,8] or sulfides,[13,20] respectively. In laboratory experiments, it was shown that, depending on conditions such as pH and concentrations of dissolved Fe(II) and sulfide, their transformation can lead to either Fe–sulfide formation or the stabilization into more crystalline Fe-oxides like goethite.[18,19,21] In contrast, more ordered Fe-oxides, such as goethite, magnetite, and hematite, have a lower density of reactive sites and undergo sulfide-promoted reductive dissolution and Fe(II)-catalyzed recrystallization on a time scale of tens of days in the laboratory.[13,22–24] This results in a greater environmental persistence and an important role in the long-term retention of associated compounds.[3] The contrasting reactivity of lepidocrocite and goethite thus impacts their stability and transformation pathways in coastal systems.

Under sulfidic conditions, the rapid precipitation of amorphous Fe–sulfides, such as amorphous iron sulfide with unknown stoichiometry (FeS_x), potentially including mackinawite,[25] is typically favored over the formation of more ordered and stable Fe–sulfide minerals during sulfide-promoted reductive dissolution of Fe-oxides.[21,26,27] Over time, the progressive sulfidation of mackinawite can lead to the formation of greigite (Fe_3S_4) and eventually pyrite (FeS_2), which is the thermodynamic endpoint and the major Fe and S sink in marine environments.[21,28,29] Despite extensive abiotic and biotic laboratory experiments studying pyrite formation,[21,27,29–32] the mechanisms of pyrite formation, especially during early diagenesis, remain debated.[27] Generally, pyrite formation is thought to be facilitated by the presence of mackinawite and greigite[27,30] and to proceed *via* two potential mechanisms. Both mechanisms involve the dissolution of the Fe–sulfide mineral precursor to an aqueous FeS intermediate. In the polysulfide pathway, the aqueous FeS intermediate reacts with nucleophilic polysulfide to form pyrite.[27] In the H_2S pathway or Wächterhäuser reaction, the aqueous FeS intermediate reacts with dissolved H_2S.[32,33] Another potential pathway of rapid pyrite formation upon the sulfidation of Fe-oxides is the recently proposed ferric-hydroxide surface (FHS) pathway.[19] In this mechanism, surface-complexed Fe(II) on the Fe-oxide surface reacts with sulfide to form a surface-bound $Fe^{II}S_2^-$ precursor. *Via* protonation, this precursor then forms pyrite even at low degrees of oversaturation. This fast mechanism of pyrite formation appears to be strongly favored at low sulfide to dissolved Fe ratios.[17–19]

While laboratory studies have extensively examined the transformation pathways and stability of various Fe-oxides,[16,27,31,34] *in situ* studies capturing the complex interactions between Fe-oxides, sulfides, ambient porewater and natural sediment matrices are limited. Most *in situ* studies have focused on freshwater and semi-terrestrial settings like rice paddies, river floodplains and forest soils,[35–40] with few addressing coastal environments.[41,42] Intertidal sediments, characterized by regular redox cycles driven by the tides, tidal flushing, high ionic strength, typical pH values between 7 and 8, and coupled Fe and S cycles, present unique conditions that may not be fully captured in simplified laboratory systems or *in situ* studies focused on terrestrial or semi-terrestrial settings.

Here, we conducted an *in situ* study in three coastal sediments with contrasting Fe and S biogeochemistry to investigate the transformation and stability of two contrasting Fe-oxides – reactive lepidocrocite and less reactive goethite and included mackinawite, which is an important intermediate in the pathway from Fe-oxides to pyrite. By incubating ^{57}Fe-enriched Fe-oxides and mackinawite mixed with sediment inside mesh bags for 8 weeks at three field plots, we used ^{57}Fe Mössbauer spectroscopy to distinguish between recrystallization/transformation, oxidation, reduction, and sulfidation processes. This study provides insights into how environmental changes may influence Fe cycling in coastal systems and sheds light on potential mechanisms for pyrite formation under natural conditions.

Materials and methods

Field plots

Three field plots located at two field sites were used for the field experiment. Low salinity field plot Haseldorfer Marsch (HSF; 53°34′50″N, 9°39′27″E) is an intertidal flat located in the upper part of the Elbe estuary, Northern Germany (Fig. S1, further details can be found in Kubeneck *et al.*[42]). The other two field plots, characterized by contrasting sulfide conditions, were located in the intertidal flat Friedrichskoog (FKS; 54°0′42″N, 8°50′6″E; Fig. S1), situated in the lower part of the Elbe estuary and characterized by polyhaline conditions (>18 psu). One field plot was characterized by low aqueous sulfide concentrations (0–35 μM, Fig. S9, FKS-lowS). The other field plot, FKS-highS, was located approximately 7 m away from FKS-lowS and had dissolved sulfide concentrations of up to 4.4 mM (Fig. S9). Both field plots were adjacent to field plots presented by Kubeneck

 This journal is © The Royal Society of Chemistry 2025

Open Access Article. Published on 18 2025. Downloaded on 14.05.2026 20:13:44.
This article is licensed under a Creative Commons Attribution 3.0 Unported Licence.

Table 1 Key porewater characteristics at 15 cm depth at the three field plots. Dissolved SO_4^{2-} : Cl^- molar ratios are also added for the surface water at HSF and FKS. Values represent the average of porewater analysis collected at 5 to 6 time points during the experimental duration from three replicates. The full data set is presented in Section S4

	HSF	FKS-lowS	FKS-highS
E_h [mV]	72 ± 27	83 ± 50	−88 ± 88
pH	7.41 ± 0.11	7.49 ± 0.14	7.62 ± 0.25
Fe [μM]	354 ± 45	86 ± 14	11 ± 7
HS^- [mM]	0 ± 0	0.01 ± 0.02	3.4 ± 0.9
SO_4^{2-} [mM]	0 ± 0	18.3 ± 2.1	11.1 ± 1.1
P [μM]	97 ± 6	66 ± 19	47 ± 9
SO_4^{2-} : Cl^- [mol:mol]	0.00 ± 0.00	0.05 ± 0.00	0.03 ± 0.00
Surface water SO_4^{2-} : Cl^- [mol:mol]	0.22 ± 0.05	0.05 ± 0.00	0.05 ± 0.00

et al.,[43] which provide a detailed geochemical characterization of each plot. The three field plots used in this experiment cover a range of dissolved Fe and sulfide concentrations with varying salinity (Table 1 and Section S4), providing conditions to test how contrasting aqueous geochemistry impacts *in situ* transformation of lepidocrocite, goethite, and mackinawite.

Fe (oxyhydr)oxide synthesis

All glassware used for mineral synthesis was acid-washed (10% hydrochloric acid, v/v) for 24 h and then rinsed thoroughly with ultra-pure water (UPW, Milli-Q, Millipore, >18.2 MΩ cm) before use. All solutions were prepared using analytical- or higher grade chemicals.

Natural isotope abundance Fe(0) (^{NA}Fe, 10 μm particle size, Merck, isotope composition: 5.8% ^{54}Fe, 91.8% ^{56}Fe, 2.1% ^{57}Fe, and 0.3% ^{58}Fe[44]) and ^{57}Fe (96.1% purity, metallic Fe(0) powder, Isoflex) were used for mineral synthesis. For isotopically enriched lepidocrocite (30% enrichment; ^{57}Fe–Lp) and goethite (20% enrichment; ^{57}Fe–Gt) a mix of ^{57}Fe and ^{NA}Fe was dissolved in 2 M HCl overnight. For ^{57}Fe–Lp synthesis, the filtered (0.22 μm, nylon) Fe(II) stock solution was titrated to pH 6.0–6.5 with 1 M NaOH at room temperature, then oxidized under vigorous stirring and gentle purging with air (approx. 100 mL min^{-1}) while the pH was maintained by the further addition of 1 M NaOH. For ^{57}Fe–Gt, the resulting Fe(II) stock solution was oxidized with excess 30% H_2O_2 and subsequently filtered (0.22 μm nylon). Then, the pH was raised to pH 13 by adding 1 M KOH dropwise under constant stirring and the suspension was subsequently placed in an oven at 70 °C in Nalgene bottles for 60 h.[3]

All precipitates were repeatedly washed until the conductivity of the supernatant was <100 μS cm^{-1} by resuspending the precipitates in UPW centrifuging the suspensions (3500 g for 25 min) and decanting the supernatant. The washed solids were resuspended in UPW, shock frozen by dropwise addition into liquid N_2, freeze-dried, gently homogenized with a mortar and pestle, and stored in brown glass bottles in a desiccator until use.

Synthesized minerals were characterized by X-ray diffraction (XRD, Bruker D8 ADVANCE) and ^{57}Fe Mössbauer spectroscopy. Synthesized ^{57}Fe–Lp contained some Gt (15–16%) based on 77 K Mössbauer spectroscopy data and XRD (see Section S3). Mössbauer spectroscopy indicated a small amount of maghemite (MagH) present in the ^{57}Fe–Gt (~5%, see Section S3), which was undetectable by XRD and did not undergo transformations during the field experiment.

Mackinawite synthesis

Mackinawite enriched with 30% ^{57}Fe (^{57}Fe–Mkw) was synthesized in an anoxic chamber (Labmaster 130, MBraun, Germany; N_2 atmosphere, <1 ppm v/v O_2) at room temperature. 140 mL of 0.05 M Na_2S stock solution was poured into 140 mL of 0.05 M Fe stock solution, prepared by dissolving ^{NA}Fe and ^{57}Fe (2 : 1 ratio) in 2 M HCl overnight (filtered 0.22 μm nylon), under continuous stirring. A black precipitate appeared immediately and the suspension was continuously stirred for 1 d. The suspension was then centrifuged at 3500 g (20 min, room temperature) outside the glovebox. Inside the glovebox, the supernatant was discarded and the washed particles were resuspended in 20 mL UPW. The suspension was then shock-frozen by immersing the closed bottle inside liquid N_2 for a few seconds outside the glovebox and was freeze-dried (with flushing of freeze dryer by Ar to prevent potential oxidation). The dried precipitates were brought back into the glovebox, homogenized with mortar and pestle, and stored in a glass bottle inside the glovebox until use.

The synthesized mineral (^{57}Fe–Mkw) was characterized by XRD and ^{57}Fe Mössbauer spectroscopy. XRD identified the mineral as mackinawite (Section S3), while Mössbauer spectroscopy (5 K) indicated the presence of mackinawite (52%) and disordered FeS_x (48%, see Section S3 for further details).

Preparation of mesh bags and sample holders

Mesh bags (dimensions ~1 × 2 cm) were prepared from polyethylene terephthalate mesh fabric (51 μm pore size, SEFAR, Switzerland) for the incubation of sediment–mineral mixes. The mesh fabric sheets were double-layered, folded and heat-sealed on two sides before filling. For mineral–sediment mixes, 30 mg of ^{57}Fe–Lp or ^{57}Fe–Gt or ^{57}Fe–Mkw were thoroughly homogenized with 300 mg of sieved sediment using mortar and pestle before transferring the mixes into the mesh bags (further information on used sediment can be found in Section S2). Mineral addition to the sediment increased the total Fe content of the sediment by a factor of 7.5, ensuring that >98% of total ^{57}Fe in the mineral–sediment mixes originated from the added

Open Access Article. Published on 18 2025. Downloaded on 14.05.2026 20:13:44.
This article is licensed under a Creative Commons Attribution 3.0 Unported Licence.

^{57}Fe-enriched minerals. The filled mesh bags were then placed into 3D-printed acrylic sample holders with a 3.5 cm long opening,[45] ensuring sufficient contact between the mesh bag and water-saturated sediment. A threaded labeled nylon rod was screwed onto the sample holder containing the sample to allow easy insertion and retrieval of the samplers in the field. To avoid oxidation artifacts, Mkw mesh bags and sample holders were prepared in an anoxic glovebag (N_2-atmosphere) and transported to the field in air-tight, double-sealed, N_2-flushed aluminum bags. Prepared sample holders with mesh bags containing Lp or Gt were vacuum-sealed for transportation.

Sample installation and removal

At each field site, 6 samples (3 mineral–sediment mixes in duplicate) were installed at 15 cm sediment depth for 8 weeks in Summer 2021 (August to September). Samples containing the same mineral (*e.g.* two ^{57}Fe–Lp–sediment mixes) were installed in parallel with a distance of ~20 cm (Fig. S2). The three resulting lines (one line per mineral) were arranged as a triangle in the field (Fig. S2). For installation, sample holders were removed from the vacuum-sealed bags and pushed into the sediment. The installation of oxygen-sensitive samples in the field followed the methodology presented by Kubeneck *et al.*[43] Briefly, to avoid the oxidation of samples containing Mkw, a 15 cm long core liner (UWITEC, PVC-corer, 8.6 cm diameter) was pushed 2 cm into the sediment, and the headspace of the core liner was vigorously flushed with N_2 for ~3 minutes. Samples containing Mkw were removed from the air-tight Al-bags and pushed into the sediment under the N_2-atmosphere inside the core liner.

At the end of the experiment, after 8 weeks, all samples were still in place and only minor erosion and/or plant debris collection was observed.[43] With the help of the nylon rod, the samples were pulled out, cut from the nylon rods, and immediately vacuum sealed (Fosa Vacuum bags, Malaga series) and stored on ice. Sample holders were covered by wet sediment, which likely further protected the sample from oxidation. Within ~5 h, recovered samples were additionally sealed in air-tight, N_2-flushed double-sealed Al-bags containing O_2 absorbers and kept at −20 °C and transported frozen back to the laboratory at ETH Zurich on ice, where they were further processed.

Field site characterization

During the experiment, sediment temperature, oxidation–reduction potential (ORP) and porewater composition were regularly monitored, as described by Kubeneck *et al.*[43] Briefly, every 7 to 10 days, sediment temperature was recorded at ~10 cm depth in the center of the field plots. ORP was measured using a custom-made probe with a platinum electrode inserted into the water-saturated sediment, and an AgCl reference electrode (supersaturated KCl, Paleo Terra, The Netherlands) placed in the overlying surface water to promote electrode stabilization and reduce junction potential artifacts. The platinum tip was cleaned with steel wool prior to use, and the electrodes were allowed to stabilize for at least 30 minutes before readings were recorded. ORP values were corrected for temperature and converted to redox potential (E_h) relative to the standard hydrogen electrode. At HSF and FKS-highS, ORP was recorded in the center of the experimental plot, while at FKS-lowS, the electrode was installed approximately 2 meters from the plot center. Given the known challenges of measuring absolute E_h in mineral-rich, heterogeneous environments, these values are interpreted as showing general trends concerning the redox conditions rather than precise values.

In addition, MacroRhizons (Rhizosphere, The Netherlands) with a 5 cm long porous tip (0.15 μm pore size) were used to collect porewater samples in the center of the experimental plot (two MacroRhizons per field plot) at a sediment depth of 15 cm, matching the burial depth of the samples. The MacroRhizons were installed at each sampling event (two per field plot) and removed after collection, rather than remaining in the field throughout the experiment. To remove any O_2 from the tubing of the MacroRhizons, the first 2 mL of porewater was discarded. Afterward, porewater was collected for major elemental and anion analysis, dissolved organic carbon (DOC), total nitrogen (TN), sulfide, pH, and alkalinity. First, ~3 mL of porewater was collected into pre-acidified (30 μL ultra-high purity, concentrated nitric acid) crimp vials, which were stored at 4 °C until analysis for major elemental concentrations (Ca, Mg, Fe, Mn, K, Na, Si, P, S) by inductively coupled plasma optical emission spectrometry (ICP-OES, Agilent 5100). The next ~0.5 mL of porewater was collected into crimp vials containing 2 mL of 2% zinc acetate solution for dissolved sulfide analysis. These samples were also stored at 4 °C until analysis by the methylene blue protocol.[46] Porewater volumes were precisely determined through gravimetric analysis after sample collection. For major anion, DOC, TN, pH and alkalinity analyses, porewater was collected into another crimp vial. Within 8 h, a subsample was acidified with 0.1 M HCl to pH 3–4 and stored at 4 °C for later DOC and TN analysis (DOC analyzer, Dimatoc 2000, Dimatec). Total alkalinity was determined in a 2 mL aliquot of the porewater samples using 0.01 M HCl *via* a two-step titration and pH was determined with a double-junction electrode (3 M KCl, Metrohm AG, Switzerland). Another subsample (0.5 mL) was taken for major anion analysis and frozen (−20 °C) until analysis. After thawing the major anion samples, ion chromatography (IC, Metrohm 940 Professional IC Vario) was used to determine the concentrations of Cl^-, Br^-, F^-, and SO_4^{2-}.

For additional field site characterization, porewater depth profiles were collected at the end of the field experiment (see Section S1.6.1). To gain insights into the temporal and (micro) spatial distribution of sulfide at the field plots, we installed passive DGT samplers for dissolved sulfide species (binding layer of AgI, DGT® Research, further details Section S1.6) at three time points during the experiment (beginning, middle, end).

Porewater species concentrations (pH, alkalinity, dissolved sulfides, major elemental and anion concentrations) were used to calculate saturation indices (SI) of pyrite and mackinawite with VisualMINTEQ (Version 3.1) using the default database (thermo.vdb, comp_2008.vdb). The equilibrium constants were corrected for sediment temperature, and ionic strength was calculated using the Davies equation for ion activity corrections.

 This journal is © The Royal Society of Chemistry 2025

Open Access Article. Published on 18 2025. Downloaded on 14.05.2026 20:13:44.
This article is licensed under a Creative Commons Attribution 3.0 Unported Licence.

The SI values reported in this paper were based on calculations in which oversaturated solids were not allowed to precipitate.

Solid phase analysis

Samples were freeze-dried in an Ar-flushed freeze dryer. After drying, the surrounding sediment was removed from the sample holders inside an anoxic glovebox, and the mesh bags were recovered from the sample holder. The solid-phases were homogenized with an agate mortar and pestle, and stored in glass vials in the anoxic chamber until further processing.

Mössbauer spectroscopy. Mössbauer spectra were collected using a ^{57}Co/Rh γ-radiation source in constant acceleration mode in transmission setup (WissEl, Wissenschaftliche Elektronik GmbH) for initial minerals and dried reacted samples. Approximately 20–40 mg of the sample was sealed between two Kapton tape strips inside an anoxic chamber and stored there until immediately before analysis. For certain samples, duplicates were measured and revealed no substantial difference among the samples (see Section S6.2). The samples were measured at 77 and 5 K inside a closed-cycle He cryostat (SHI-850, Janis Research Co.). Spectra were calibrated with an α-Fe(0) foil at 295 K. The Lorentzian half width at half maximum was set according to the broadening of the inner doublet of the calibration foil at 295 K and collected spectra were normalized to 1 with respect to absorption. Fitting was done using Recoil software (University of Ottawa, Canada) using an extended Voigt-Based fitting (xVBF) routine.[47,48] ^{57}Fe Mössbauer spectroscopy almost exclusively detected the signal of the ^{57}Fe coming from the added ^{57}Fe–Lp or ^{57}Fe–Gt or ^{57}Fe–Mkw in the mineral–sediment mixes, as the minerals contributed >98% to the total ^{57}Fe content in the initial sample.

Results and discussion

Aqueous geochemistry of field plots

Porewater data were collected from the field plots every 7 to 10 days throughout the experiment to assess how contrasting geochemical conditions influence *in situ* mineral transformations (Table 1, Fig. S9 and Section S4). Field plots HSF and FKS-lowS exhibited similar E_h values at 15 cm sediment depth (average 72–83 mV, Table 1 and Fig. S9A), suggesting Fe-reducing conditions at porewater pH of ∼7.45.[49] This is further supported by the presence of dissolved Fe in the porewater (Table 1 and Fig. S9B), with HSF having higher concentrations (354 μM) compared to FKS-lowS (86 μM). Given these E_h values, sulfate reduction should be marginal at HSF and FKS-lowS.[49] This aligns with the absence of dissolved sulfide at HSF and FKS-lowS. However, differences in sulfate reduction activity between the plots were suggested by the molar ratio of dissolved SO_4^{2-} : Cl^- (Table 1). Assuming Cl^- behaves as a conservative tracer, changes in the ratio of dissolved SO_4^{2-} : Cl^- from surface water to porewater indicate sulfate removal at depth.[50,51] At HSF, this ratio approached 0 at 15 cm depth, indicating sulfate removal (Fig. S9). Additionally, a color change in passive DGT samplers, installed midway and at the end of the experiment, indicated the presence of dissolved sulfides at specific time points and microsites, further supporting the occurrence of sulfate reduction (Fig. S18). Conversely, the SO_4^{2-} : Cl^- ratio in the porewaters at FKS-lowS remained consistent with surface water values, suggesting negligible sulfate reduction (Table 1). This is corroborated by the lack of color change in the DGT samplers even after 24 hours of installation (Fig. S19).

In contrast, the third field plot, FKS-highS, displayed different geochemical conditions. E_h values were consistently lower (−88 mV; Table 1 and Fig. S9), and pH values were higher (7.62), indicating sulfate-reducing conditions.[49] Low dissolved Fe (4 to 18 μM) indicated the scavenging of dissolved Fe by dissolved sulfide, which was further supported by the oversaturation of the porewater with respect to mackinawite and pyrite (Fig. S21). High dissolved sulfide concentrations (2.0 to 4.4 mM) were consistent with ongoing sulfate-reduction as suggested by low E_h values and lower SO_4^{2-} : Cl^- ratios at depth compared to surface water samples (Table 1). Passive DGT samplers turned black within 30 minutes of installation, confirming the presence of dissolved sulfides (Fig. S20).

Limited transformation of lepidocrocite and goethite under low S, Fe-reducing conditions

The 5 K Mössbauer spectrum of the initial ^{57}Fe–Lp mixes revealed two sextets: one with a narrow hyperfine field (43.0 T) consistent with lepidocrocite,[39,52] and another with a wider hyperfine field (49.5 T), corresponding to goethite[24] (Fig. 1A and Table 2). The Fe atoms present in goethite contributed 14% to the spectral area in the 77 K Mössbauer spectrum (Fig. S7 and Table S3). The contribution of Gt to the remaining ^{57}Fe in the ^{57}Fe–Lp mixes barely changed during the incubation at HSF or FKS-lowS, suggesting the inherent stability of goethite (Fig. 1C, E and Table 2).

At the low salinity field plot HSF, Mössbauer data showed limited transformation of lepidocrocite, with about 20% of the ^{57}Fe in the mesh bags transforming into secondary minerals (Fig. 1C and E). The 77 K Mössbauer data revealed that 16% of the ^{57}Fe in the mesh bags pool was Fe(II), evidenced by a doublet with hyperfine parameters typical of solid-phase Fe(II) (Fig. S26C and Table S5). The Fe(III) was either associated with goethite, as indicated by a sextet at 77 K, or in a magnetically unordered phase, which may represent lepidocrocite, ferrihydrite, or other Fe(III) minerals with a Néel temperature below 77 K.[53] The 5 K Mössbauer spectrum was dominated by two sextets with hyperfine parameters consistent with lepidocrocite and goethite (Fig. 1C and Table 3).[24,52] Based on the spectral contribution of the two sextets, 57% of the ^{57}Fe in the mesh bags was associated with lepidocrocite and 26% with goethite, indicating ∼10% increase in the goethite pool with incubation. Additionally, the Fe(II) doublet observed in the 77 K spectrum was no longer present at 5 K. Instead, at 5 K we observed a collapsed feature contributing the same spectral area (17% spectral area, Fig. 1C and Table 3). This suggests that the collapsed feature was mainly Fe(II), with potentially some minor Fe(III), which is not magnetically ordered. Such a disordered phase could be Fe(II) complexed by organic matter, bound in amorphous Fe–sulfide minerals like FeS_x, a green-rust-like phase, or other ferrous

Open Access Article. Published on 18 2025. Downloaded on 14.05.2026 20:13:44.
This article is licensed under a Creative Commons Attribution 3.0 Unported Licence.

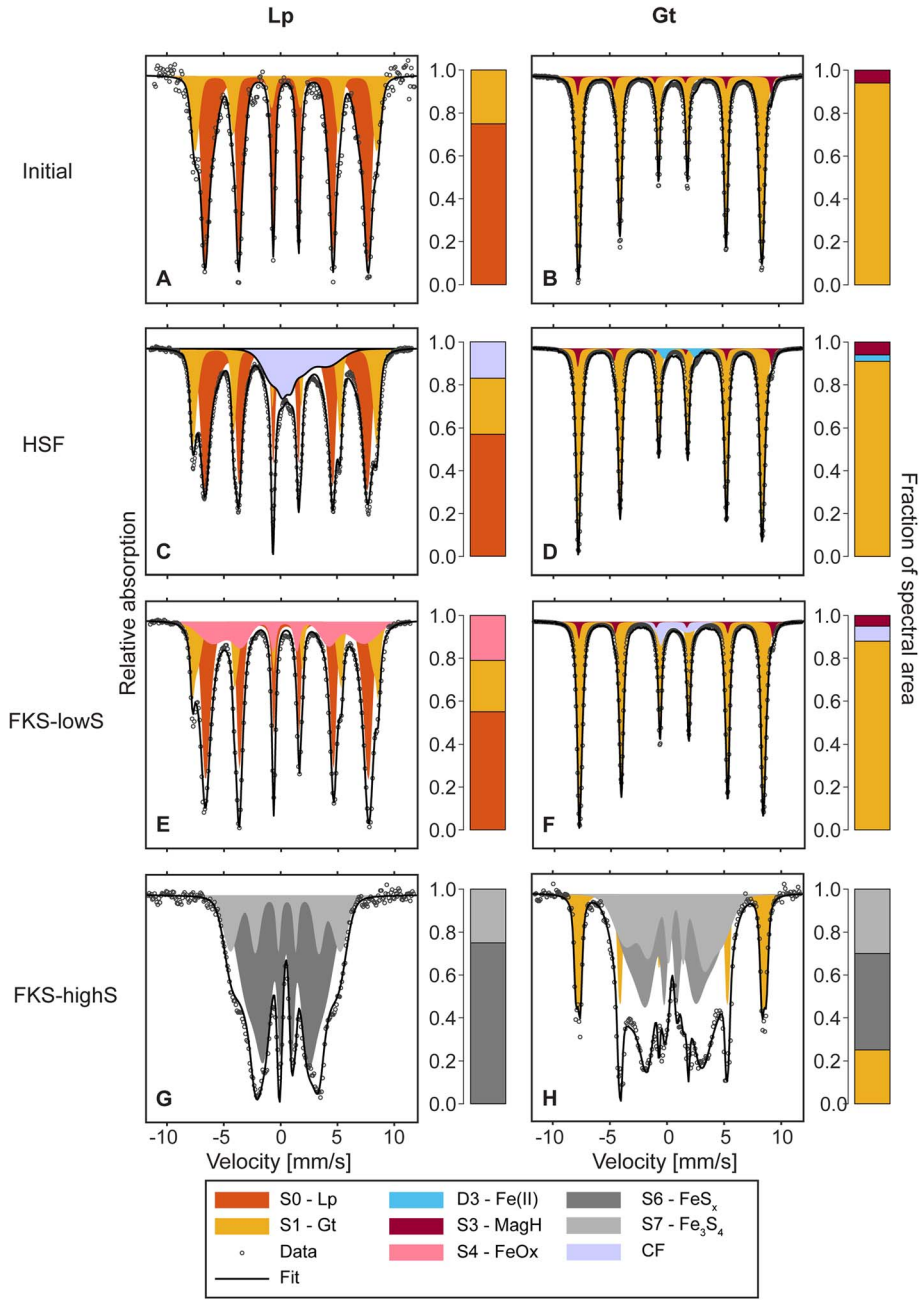

Fig. 1 Fitted 5 K Mössbauer spectra of initial mineral–sediment mixes of ^{57}Fe–Lp (A), ^{57}Fe–Gt (B) and reacted mineral–sediment mixes (C–H) incubated at the three field plots. Bar graphs to the right of the Mössbauer spectra show spectral fractions of different fitted mineral phases. Fitted hyperfine parameters are presented in Table 2. Abbreviations: S = sextet; D = doublet; Lp = lepidocrocite; Gt = goethite; MagH = maghemite; FeO_x = amorphous iron oxyhydroxide; FeS_x = amorphous iron sulfide; Fe_3S_4 = greigite; CF = collapsed feature; HSF = Haseldorfer Marsch; FKS-lowS = low sulfide plot Friedrichskoog; FKS-highS = high sulfide plot Friedrichskoog.

minerals,[32,39,53,54] indicating the partial reductive dissolution of the incubated lepidocrocite.

The presence of a green-rust-like phase was also indicated by an alternative fitting approach using the full static Hamiltonian model,[55] where an octet with hyperfine parameters matching solid-phase Fe(II) in green rust contributed to 17% to the spectrum (Section S6.1).[53] Thus, two different fitting approaches suggest that the reductive dissolution likely resulted in the formation of a green-rust-like phase. Additionally, we cannot rule out the presence of minor amounts of pyrite, as our second alternative fit of the 77 K and 5 K Mössbauer spectra of ^{57}Fe–Lp mixes at HSF suggests the formation of minor amounts of pyrite (3–4%, Fig. S28 and Table S7) alongside a green-rust like phase. However, pyrite can often not be distinguished from other paramagnetic Fe(III) phases, such as clay minerals, and thus its presence remains ambiguous.

At high salinity, low sulfide field plot FKS-lowS, most of the lepidocrocite appeared unchanged after incubation, with 25%

 This journal is © The Royal Society of Chemistry 2025

Open Access Article. Published on 18 2025. Downloaded on 14.05.2026 20:13:44.
This article is licensed under a Creative Commons Attribution 3.0 Unported Licence.

Table 2 Hyperfine parameters of fitted 5 K Mössbauer spectra of reacted ^{57}Fe–Lp and ^{57}Fe–Gt mineral–sediment mixes. Fitting lepidocrocite and goethite sometimes required multiple components indicated by H1, H2, and the fractional contribution of H2 (Frac. H2). Fe(II) in doublet 3 (D3) represents non-sulfide Fe(II). Parameters fixed during the fitting process are marked in bold. Fitted hyperfine parameters for initial ^{57}Fe–Lp and ^{57}Fe–Gt are presented in Table S3[a]

Mineral	Field plot	Component	CS [mm s^{-1}]	QS or ε [mm s^{-1}]	σ_{QS} or σ_ε [mm s^{-1}]	H [T]	σ_H [T]	Area [%]	Red. χ^2
^{57}Fe–Lp	HSF	S1 – Gt	0.49	−0.09		49.92		26	*13.94*
		H1				**50.60**	**1.0**		
		H2				**49.00**	1.8		
		Frac. H2				*43.4%*			
		S0 – Lp	0.49	0.02		43.12		57	
		H1				**44.61**	**1.9**		
		H2				**40.00**	**4.0**		
		Frac. H2				*32.40%*			
		CF	1.23	0.68		13.82	7.3	17	
	FKS-lowS	S1 – Gt	0.49	−0.11		48.94		24	*7.58*
		H1				**50.50**	**0.5**		
		H2				**48.00**	**2.0**		
		Frac. H2				*62.3%*			
		S0 – Lp	0.50	0.02		43.74		54	
		H1				**44.40**	**1.6**		
		H2				**41.00**	**1.8**		
		Frac. H2				*19.5%*			
		S4 – FeO_x	**0.5**	**0.15**		**41.00**	**7.0**	21.5	
	FKS-highS	S6 – FeS_x	0.46	−0.02		19.90	6.0	75	*1.62*
		S7 – Fe_3S_4	0.49	−0.07		29.94	3.6	25	
^{57}Fe–Gt	HSF	D3 – Fe(II)	**1.20**	**2.80**	**0.50**			3	*41.80*
		S1 – Gt	0.49	−0.12		50.41	1.1	91	
		S3 – MagH	0.55	0.19		53.20	**0.1**	6	
	FKS-lowS	S1 – Gt	0.49	−0.12		50.41	1.1	88	*36.00*
		S3 – MagH	0.54	0.19		53.20	**0.2**	5	
		CF	0.60	1.20	**5.00**			7	
	FKS-highS	S1 – Gt	0.47	−0.11		50.42		25	*4.29*
		H1				51.65	**0.6**		
		H2				49.37	**0.6**		
		Frac. H2				53.6%			
		S6 – FeS_x	0.34	0.03		21.45	**7.0**	45	
		S7 – Fe_3S_4	0.64	−0.14		25.2	**6.0**	30	

[a] Abbreviations: Temp. = temperature; CS = center shift; QS = quadrupole splitting (for doublets); ε = quadrupole shift (for sextets); σ = standard deviation of QS, ε, or H; H = hyperfine field; Red. χ^2 = reduced χ^2 – goodness of fit; D = doublet; S = sextet; Lp = lepidocrocite; Gt = goethite; MagH = maghemite; FeO_x = amorphous iron oxyhydroxide; FeS_x = amorphous iron sulfide; Fe_3S_4 = greigite; CF = collapsed feature.

Table 3 Hyperfine parameters of fitted 5 K Mössbauer spectra of reacted ^{57}Fe–Mkw mineral–sediment mixes. Fitting parameters fixed during the fitting process are marked in bold[a]

Field plot	Component	CS [mm s^{-1}]	QS or ε [mm s^{-1}]	σ_{QS} or σ_ε [mm s^{-1}]	H [T]	σ_H [T]	Area [%]	Red. χ^2
HSF	D2 – Mkw	0.46	0.07	0.32			15	*3.10*
	S4 – FeO_x	0.43	0.04		46.76	**3.3**	10	
	S6 – FeS_x (a)	0.42	−0.02		17.07	**3.0**	28	
	S7 – Fe_3S_4	0.51	0.06		**32.29**	**4.0**	10	
	CF	0.66	0.25	**20.00**			36	
FKS-lowS	D2 – Mkw	0.46	0.09	0.30			24	*2.08*
	S0 – Lp	0.40	0.09		45.97	**2.0**	5	
	S6 – FeS_x (a)	0.41	−0.02		17.03	3.4	34	
	S7 – Fe_3S_4	0.44	0.00		30.86	4.4	9	
	CF	0.45	**0.00**	**16.0**			28	
FKS-highS	S6 – FeS_x (a)	0.42	−0.05		17.72	2.9	68	*13.70*
	S7 – Fe_3S_4	0.50	−0.08		28.92	**4.0**	18	
	S8 – FeS_x (b)	0.19	0.13		7.51	1.7	14	

[a] Abbreviations: Temp. = temperature; CS = center shift; QS = quadrupole splitting (for doublets); ε = quadrupole shift (for sextets); σ = standard deviation of QS, ε, or H; H = hyperfine field; Red. χ^2 = reduced χ^2 – goodness of fit; D = doublet, S = sextet, Lp = lepidocrocite, FeO_x = amorphous iron oxyhydroxide, Mkw = mackinawite, FeS_x = amorphous iron sulfide; Fe_3S_4 = greigite; FeS_x (b) = additional amorphous iron sulfide phase.

Open Access Article. Published on 18 2025. Downloaded on 14.05.2026 20:13:44.
This article is licensed under a Creative Commons Attribution 3.0 Unported Licence.

transforming into secondary phases. However, no reduced Fe minerals were detected (Fig. 1E and S26E). Instead, a collapsed feature in the 77 K spectrum, contributing ~20% to the spectral area (Fig. S26E), became a broad sextet at 5 K with a narrow hyperfine field (~41 T, Fig. 1E and Table 2), suggesting Fe(III) bound in a highly disordered Fe-oxide phase potentially associated with organic matter.[54]

Porewater at both HSF and FKS-lowS was characterized by circumneutral pH, dissolved Fe, and no dissolved sulfide (Table 1). Previous lab experiments with Fe(II)-spiked lepidocrocite suspensions have demonstrated that lepidocrocite readily transforms into goethite under these conditions.[7,8] However, our field experiment showed minimal goethite formation in incubated ^{57}Fe–Lp mineral–sediment mixes at low salinity plot HSF (~10% increase) and none at high salinity plot FKS-lowS, suggesting that Fe(II)-catalyzed transformation was hampered or absent *in situ*. The higher dissolved Fe concentration at HSF (354 μM) compared to FKS-lowS (86 μM) may explain why transformation occurred at HSF but not at FKS-lowS, as the transformation kinetics depend on the rate of Fe(II) transport from solution to mineral surface, which is strongly dependent on the dissolved Fe(II) concentration.[7] Additionally, the dissolved Fe(II) concentrations in the field were lower than those typically used in laboratory experiments (concentration range: 0.3 to 5 mM).[6,7,24,56,57] Thus, the limited Fe(II)-catalyzed transformation of lepidocrocite may relate to the lower dissolved Fe(II) concentration observed *in situ*. These low Fe(II) concentrations may also explain the absence of magnetite formation, despite pH values above 7, which are typically favorable for magnetite precipitation.[57] In contrast, Schulz *et al.*[39] reported magnetite formation during the reductive transformation of lepidocrocite incubated in mesh-bags in redox-fluctuating rice paddy soils (up to 1.5 mM Fe^{2+} in porewater), even under subneutral pH conditions. Further, lepidocrocite mixed with soil in redox-fluctuating rice paddies was completely transformed within 8 weeks,[39,40] highlighting differences in Fe mineral transformation pathways depending on the local geochemistry. We hypothesize that the combination of lower Fe(II) availability with other geochemical factors such as higher ionic strength and a complex porewater matrix containing dissolved P, Si, and organic matter (Table 1 and Section S4) further stabilized lepidocrocite against Fe(II)-catalyzed transformation. This is consistent with findings from laboratory studies,[57–60] showing for instance the limited transformation of lepidocrocite in the presence of Si.[57] Additionally compared to laboratory settings, field conditions introduce a suite of dynamic and interacting variables that may affect Fe mineral transformations, which are challenging to replicate *ex situ*. For example, natural temperature fluctuations, salinity changes and temporal changes in aqueous geochemical composition (Section S4) could all modulate Fe(II) reactivity. Additionally, the tidal redox cycling may periodically reoxidize Fe(II), which could stabilize and/or facilitate new lepidocrocite formation.[39] Thus, these complex and interdependent field-specific conditions likely contribute to the persistence of lepidocrocite in our studied field sites. Overall, our results suggest that at dissolved Fe(II) concentrations typical for coastal porewaters, Fe(II)-catalyzed transformation of lepidocrocite is minor, resulting in conditions under which lepidocrocite may persist over periods of weeks.

The E_h values and dissolved Fe at HSF and FKS-lowS suggested active Fe-reduction, which would typically promote the reductive dissolution of lepidocrocite. However, the formation of mixed-valence or reduced Fe minerals was absent at FKS-lowS and minor at HSF. This contrasts with earlier findings at HSF, where ^{57}Fe-labeled ferrihydrite mixed with sediment was nearly fully reduced within 7 weeks, with green rust as the dominant secondary mineral.[42] Assuming similar trends in microbial activity, as indicated by similar porewater geochemical conditions, this suggests that other poorly crystalline Fe phases, such as ferrihydrite, likely present in the bulk sediment at HSF[42] and FKS-lowS,[43] were preferentially reduced over the added lepidocrocite. Additionally, it might indicate that the (microbially driven) reductive dissolution of lepidocrocite *in situ* is substantially slower than in laboratory-based studies, where lepidocrocite dissolves within hours.[61] Further it contrasts with a recent field study in a rice paddy soil showing about 80% transformation of lepidocrocite to goethite and mixed-valence Fe-minerals after 16 weeks.[40] Potentially, the combination of low sulfide conditions, high pH, and presence of organic matter at HSF and FKS-lowS create ideal conditions stabilizing lepidocrocite[62] and thus limiting reductive dissolution and Fe(II)-catalyzed transformation, allowing the persistence of lepidocrocite in Fe-reducing, low sulfide coastal sediments.

At the low salinity field plot HSF, the low dissolved molar ratio of SO_4^{2-} : Cl^- and the detection of dissolved sulfide in DGT probes (Section S1.6.2) suggest the occurrence of sulfate reduction in microsites, potentially leading to lepidocrocite sulfidation and the formation of Fe–sulfide minerals such as FeS_x, greigite, or pyrite. Although we cannot unambiguously confirm the formation of Fe–sulfides, the collapsed feature in the 5 K Mössbauer spectrum of the ^{57}Fe–Lp mineral–sediment mix may partially represent such phases in addition to green rust. An alternative fitting approach (Section S6.1) also suggested minor amounts of pyrite; however, the pyrite doublet may equally represent Fe(III) bound in clay minerals, making this interpretation tentative. While fast pyrite nucleation at environmental conditions is unusual,[29–31] rapid pyrite formation may have occurred *via* the FHS pathway.[19] This mechanism was hypothesized to be particularly important in environments containing high concentrations of ferric iron and low sulfide.[18] These conditions are present in the ^{57}Fe–Lp mixes incubated at HSF and may explain minor sulfidation of added lepidocrocite. This mechanism could explain how pyrite present in the bulk sediment of HSF may have formed.[42]

In contrast to changes observed in the incubated ^{57}Fe–Lp mixes at HSF and FKS-lowS, ^{57}Fe–Gt mixes were nearly unchanged, indicated by similar Mössbauer spectra for initial and reacted ^{57}Fe–Gt mixes dominated by a sextet (S1-Gt) at 77 and 5 K with hyperfine parameters consistent with crystalline goethite (Fig. 1B, D, F, S26B, D, F and Tables S5, 2).[24,52] The stability of goethite aligns with Fe(II)-spiked goethite suspension experiments[63] and further suggests that sufficient other Fe minerals were present in the bulk sediment, which were

 This journal is © The Royal Society of Chemistry 2025

Open Access Article. Published on 18 2025. Downloaded on 14.05.2026 20:13:44.
This article is licensed under a Creative Commons Attribution 3.0 Unported Licence.

preferentially reductively dissolved. However, we cannot exclude that a minor fraction underwent atom exchange, which may have occurred with the surrounding porewater.[64] Overall, the results indicate a low *in situ* reactivity of lepidocrocite and goethite in non-sulfidic, Fe-reducing coastal sediments, suggesting that both minerals may persist in those environments. The low reactivity of goethite matches field observations of nano-goethite being the most common Fe-oxide mineral in various sedimentary environments.[65]

Presence of S drives lepidocrocite and goethite transformation

At field plot FKS-highS, sulfate reduction was likely the dominant anaerobic microbial respiration pathway, as indicated by high dissolved sulfide concentrations in the porewater (Table 1). Consequently, we expected the sulfidation of the added ^{57}Fe-oxides. After 8 weeks of incubation, the lepidocrocite in the ^{57}Fe–Lp sediment–mineral mix was fully transformed. The Mössbauer spectra of the incubated mix showed the disappearance of lepidocrocite and goethite sextets, replaced by two new sextets (Fig. 1A *vs.* Fig. 1G). The new sextets (S6 – FeS_x and S7 – Fe_3S_4) contributed 75% and 25% to the spectral area, respectively, and had hyperfine parameters consistent with FeS_x and greigite, respectively (Table 2).[32,66,67] In contrast, 25% of goethite was still present in the ^{57}Fe–Gt mix after 8 weeks. The ^{57}Fe was present as FeS_x and greigite (45% and 30%, respectively, Fig. 1H). These results suggest that *in situ* sulfidation of lepidocrocite and goethite led to the formation of FeS_x and greigite, with the extent of transformation differing between the two minerals.

Dissolved sulfide, present in the surrounding porewater at high concentrations (2 to 4 mM, Fig. S9), was likely oxidized at the Fe-oxide surface. This oxidation released Fe(II) into the solution, which could then react with additional porewater sulfide to produce FeS_x,[13,22] which was oversaturated in the porewater (saturation index >0, Fig. S21). The formation of FeS_x or mackinawite upon sulfidation of lepidocrocite and goethite is consistent with laboratory findings[12,13,15,19] and a recent field study that incubated lepidocrocite in gel samplers in sulfide-rich tidal flats.[41] Interestingly, while Kraal *et al.*[41] did not observe greigite formation in their field study, our results show that greigite formed readily during the sulfidation of both Fe-oxide minerals. As greigite nucleation and crystal growth from solution are limited,[27] we hypothesize that the greigite formed from FeS_x, which precipitated immediately upon sulfidation of lepidocrocite and goethite.[20] This FeS_x then reacted with other zero-valent sulfur species or polysulfides, likely present in the surrounding porewater, to form greigite.[30,68] This aligns with our observations, where mackinawite transformed into greigite (see following section for detailed discussion). The direct contact of the Fe-oxides with the sediment likely accelerated these transformations, a condition not present in the gel samplers used by Kraal *et al.*[41]

While both lepidocrocite and goethite underwent similar transformation pathways, the transformation extent differed. Lepidocrocite was fully transformed after 8 weeks, while goethite remained partially unreacted (25%). Due to a lack of temporal sampling, we cannot pinpoint the exact rate of *in situ* lepidocrocite sulfidation. A previous laboratory study showed that lepidocrocite had a half-life of 10.9 hours with 1 mM sulfide at pH 7.5.[13] Other studies showed incomplete lepidocrocite sulfidation over 2 weeks, depending on sulfide concentrations.[17–19] Similarly, Kraal *et al.*[41] observed incomplete sulfidation of lepidocrocite incubated in gel samplers. These results contrast with our findings, which show the complete transformation within 8 weeks when lepidocrocite was mixed with the sediment. We hypothesize that mixing the lepidocrocite with sediment and incubating the mix in permeable mesh bags allowed porewater, providing high concentrations of sulfide, to flow through and react with the lepidocrocite easily. Additionally, sulfate reduction could occur inside the mesh-bag, further removing diffusion limitations. The slower transformation of goethite, as expected from laboratory studies,[13,18,22] is likely due to its higher thermodynamic stability, lower minerals' surface area and sites. Additionally, competitive adsorption of major seawater solutes has been shown to retard goethite sulfidation more than lepidocrocite sulfidation.[13] This could further explain why goethite was still present after 8 weeks of incubation at FKS-highS.

Despite the near-complete sulfidation of both minerals, no pyrite was detected in the Mössbauer spectra, even though the porewater was oversaturated with respect to pyrite (saturation index >15, Fig. S21). The high degree of oversaturation may suggest the potential of immediate pyrite precipitation, as observed in other highly reducing salt marsh environments.[9,11,69] However, unlike the salt marsh environments where immediate pyrite precipitation was favored by low pH values (5–6),[9] FKS-highS exhibited elevated pH values (>7.5, Table 1). Additionally, the porewater was oversaturated with respect to mackinawite (Fig. S21). Consequently, the fast precipitation of mackinawite likely outcompete pyrite nucleation which is kinetically hindered.[21,70] The formed FeS_x, including mackinawite, is metastable with respect to greigite,[33] resulting in the subsequent solid-state transformation to greigite. At FKS-highS the presence of *Spartina* grass might have provided oxic microsites in the reducing sediment. Redox oscillations accompanied with slightly alkaline porewater conditions (Fig. S9) favor greigite formation and stabilize it.[27,70] Simultaneously, these environmental parameters likely hindered or slowed down pyrite formation at FKS-highS.[32,70,71] Thus, our results align well with previous observations in similar environments where direct pyrite nucleation rarely occurs. Instead, pyrite likely forms from a transformation sequence involving amorphous Fe–sulfide minerals, mackinawite, and greigite.[21,26,27,31,72]

In summary, our results at FKS-highS indicate that the presence of high sulfide concentrations drove the transformation of lepidocrocite and goethite into FeS_x and greigite. Given the environmental conditions at FKS-highS and the presence of pyrite in the bulk sediment,[43] we expect that pyrite would eventually have formed in our incubated mesh-bags, *via* the polysulfide pathway.[72]

No detectable pyrite formation upon mackinawite transformation

Incubation of ^{57}Fe–Lp and ^{57}Fe–Gt mineral–sediment mixes in sulfidic conditions demonstrated that both Fe-oxides

Open Access Article. Published on 18 2025. Downloaded on 14.05.2026 20:13:44.
This article is licensed under a Creative Commons Attribution 3.0 Unported Licence.

transformed to FeS_x under sulfidic conditions, which likely further transformed into greigite. This transformation sequence may eventually lead to pyrite formation. To explore whether this pathway is reproducible starting from an intermediate phase, we also incubated ^{57}Fe–Mkw mineral–sediment mixes.

Initially, the ^{57}Fe–Mkw sample exhibited a doublet (D2) with a very small quadrupole splitting (QS) nearly resembling a singlet in the 5 K Mössbauer spectrum, consistent with stoichiometric mackinawite,[32] alongside a broad feature attributed to nonstoichiometric amorphous iron sulfide (FeS_x; Fig. 2A and Table S6).[32] These two phases could not be distinguished in the XRD spectrum (Fig. S5), suggesting that the FeS_x phase likely includes mackinawite with excess S.[19,25]

At low salinity field plot HSF, the 5 K Mössbauer spectrum of the reacted ^{57}Fe–Mkw–sediment mix showed a decrease in mackinawite (from 52% to 15%), indicating substantial transformation (Fig. 2B and Tables 3, S3). The 77 K spectrum revealed a doublet (Fe(II) D3) consistent with solid-phase or sorbed Fe(II) not associated with sulfides, two sextets (S6 and S7) corresponding to FeS_x and greigite, respectively, and a collapsed feature, likely representing a highly disordered Fe-phase.[39] At 5 K, an additional sextet (S4) emerged, likely corresponding to a mixture of lepidocrocite and ferrihydrite.[24] Greigite and the Fe-oxide phase contributed 10% each to the total spectral area.

At the high salinity field plot FKS-lowS, the transformation products and fractions were similar to HSF. Mackinawite persisted in the reacted sample after incubation (24% of the spectral area at 5 K) (Fig. 2C and Table 3). A collapsed feature contributed 28% to the spectral area of the ^{57}Fe in the mesh bags. Additionally, two sextets resembling FeS_x and greigite emerged, each contributing 34% and 9% to the spectra, respectively. Similar to HSF, an Fe-oxide formed upon mackinawite transformation, which resembled lepidocrocite and contributed 5% to the total spectral area.[52,57]

In contrast, at the sulfidic field plot FKS-highS, the features of the initial mackinawite were absent in the Mössbauer spectra after incubation, implying a complete loss of ordered mackinawite. Instead, a sextet with hyperfine parameters consistent with greigite contributed ~18% to the spectral area. The remaining spectrum was dominated by two sextets representing likely nonstoichiometric FeS_x minerals (Fig. S27F, G and Table S6). The broadness of these sextets (σ_H: 1.7–4, Table 3) raises the possibility of a hidden doublet, meaning the presence of pyrite cannot be definitively ruled out.

Despite undersaturation of porewater with respect to mackinawite at HSF and FKS-lowS (Fig. S21), mackinawite persisted, suggesting stabilization of the mineral phase or the presence of microsites where it remained thermodynamically stable. Passive DGT samples detected dissolved sulfide at HSF (Fig. S18), indicating microsites that could maintain mackinawite under favorable conditions. Additionally, the formation of secondary phases such as greigite and lepidocrocite might have created protective layers, shielding mackinawite from further transformation.[73]

The transformation of mackinawite to greigite and Fe-oxides suggests partial oxidation at field plots HSF and FKS-lowS. In

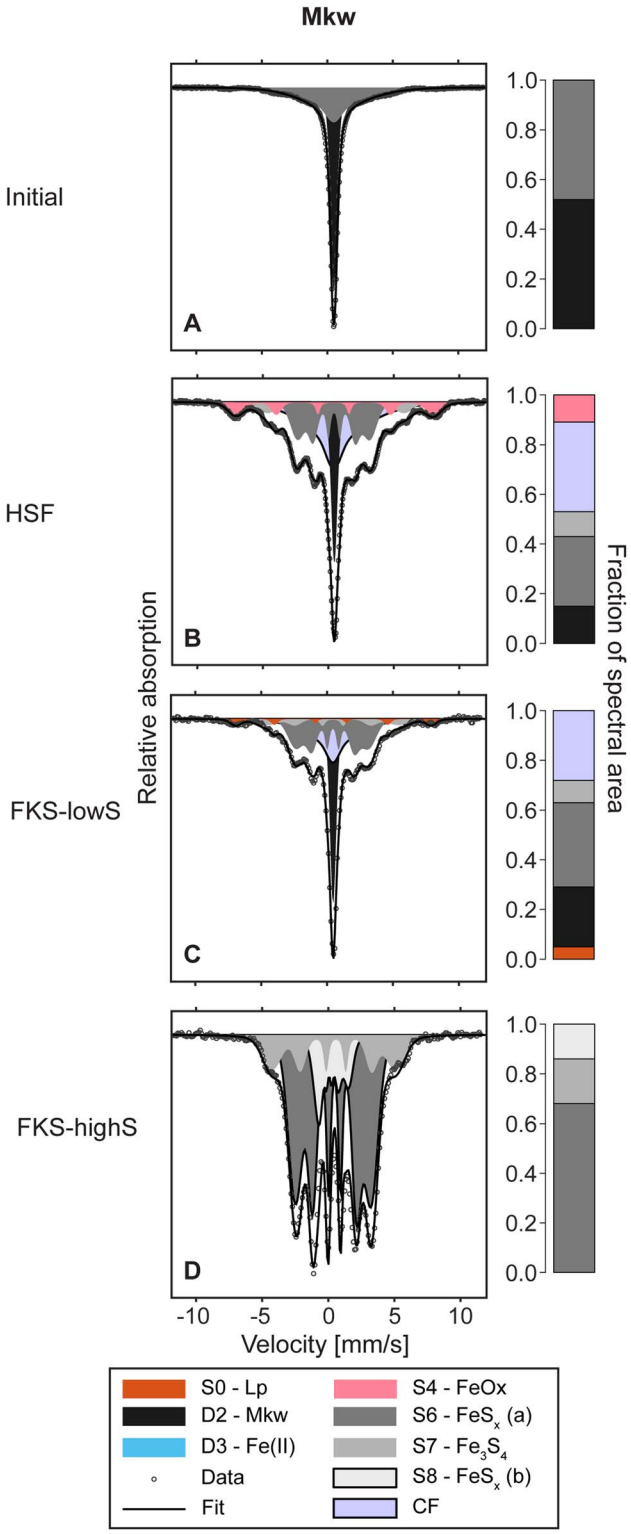

Fig. 2 Fitted 5 K Mössbauer spectra of initial mineral–sediment mixes of ^{57}Fe–Mkw (A) and reacted mineral–sediment mixes (B–D) incubated at the three field plots. Bar graphs to the right of the Mössbauer spectra show spectral fractions of different fitted mineral phases. Fitted hyperfine parameters are presented in Table 3. Abbreviations: S = sextet; D = doublet; FeO_x = amorphous iron oxyhydroxide; Mkw = mackinawite; FeS_x (a) = amorphous iron sulfide; Fe_3S_4 = greigite; FeS_x (b) = additional amorphous iron sulfide phase with different hyperfine parameters; CF = collapsed feature; Lp = lepidocrocite; HSF = Haseldorfer Marsch; FKS-lowS = low sulfide plot Friedrichskoog; FKS-highS = high sulfide plot Friedrichskoog.

This journal is © The Royal Society of Chemistry 2025

Open Access Article. Published on 18 2025. Downloaded on 14.05.2026 20:13:44.
This article is licensed under a Creative Commons Attribution 3.0 Unported Licence.

laboratory settings, mackinawite oxidation often yields lepidocrocite and elemental sulfur.[73–75] Although elemental sulfur could not be detected with our techniques, the formation of an Fe-oxide phase likely containing lepidocrocite indicates that mackinawite oxidation *in situ* followed a similar pathway to *ex situ* conditions. The presence of greigite, an intermediate in the mackinawite-to-pyrite pathway,[68] suggests the involvement of other oxidants than H_2S facilitating mackinawite transformation.[30]

The thermodynamic instability of mackinawite at HSF and FKS-lowS might also result in its dissolution, followed by the precipitation of other reduced Fe minerals such as vivianite and siderite.[76] At HSF, the porewater was oversaturated with respect to both mineral phases.[42] The 77 K Mössbauer spectrum may indicate possible vivianite formation, with an Fe(II) doublet (D3) showing hyperfine parameters close to those reported for vivianite (Table S6).[42,77] Additionally, the presence of a collapsed feature in the 5 K Mössbauer spectra suggests the presence of a disordered Fe phase or an Fe-phase present in partially ordered octets. This phase could include a green-rust like phase as has been observed to form upon vivianite incubation in field plot FKS-lowS.[43] Green rust formation has also been observed at field plot HSF.[42] Thus, we hypothesize that the collapsed feature observed in the Mössbauer spectra of the reacted ^{57}Fe–Mkw sediment mix may correspond to a green-rust-like phase or other reduced Fe minerals, such as vivianite.

At FKS-highS, the porewater was in equilibrium or slightly oversaturated with respect to mackinawite (Fig. S21). Combined with high dissolved sulfide concentrations and likely polysulfides, indicated by the whitish porewater color, we hypothesized the sulfidation of mackinawite to stable Fe–sulfide minerals such as pyrite. However, no pyrite was detected after 8 weeks, with mackinawite transforming into greigite and amorphous FeS_x minerals. This indicates that while sulfur compounds reacted with mackinawite, pyrite formation did not occur. The amorphous FeS_x minerals observed may be intermediates in a slow pyrite formation pathway.[21,26,30] The greigite formation highlights that mackinawite transformed *in situ* into a known precursor of pyrite.[68] Observations of greigite formation across all incubated ^{57}Fe-enriched minerals at high sulfide conditions (FKS-highS) suggest a consistent transformation pathway. Initially, FeS_x or mackinawite forms in our studied field conditions which then reacts further to greigite, with the potential for pyrite formation *via* a subsequent transformation sequence. The absence of pyrite in our 8 week incubation underscores the slow nature of *in situ* pyrite formation, highlighting the need for extended studies to fully observe this process.[27]

Conclusions

The results of this study provide new insights into the behavior of Fe minerals in coastal sediments with contrasting Fe and S biogeochemistry. Notably, under low sulfide, Fe reducing conditions, lepidocrocite underwent minimal Fe(II)-catalyzed transformation and reductive dissolution. These results suggest that lepidocrocite may persist longer in coastal sediments than previously anticipated based on laboratory and field studies.[8,39–41,57] Similarly, goethite appeared unchanged after 8 weeks of incubation. These findings may imply that contaminants and nutrients sorbed to lepidocrocite and goethite may remain immobilized even under Fe-reducing conditions. However, while both Fe-oxides appear stable, the interaction with porewater components, including Fe(II), may still influence their redox potential[78,79] potentially affecting their capacity to act as sorbents or reductants for trace contaminants.

In contrast, under high sulfide conditions, both lepidocrocite and goethite transformed into FeS_x and greigite within 8 weeks, with lepidocrocite undergoing more extensive transformation. These findings align with previous laboratory studies, showing that lepidocrocite is more easily sulfidized than goethite.[13] The formed greigite likely formed from FeS_x minerals that immediately formed upon the sulfide-promoted reductive dissolution of Fe-oxides. This hypothesis is supported by the transformation of incubated mackinawite under high sulfide conditions into greigite, further suggesting that greigite formation may be a key intermediate step in the eventual transformation to pyrite. However, the absence of detectable pyrite within the 8 week incubation period suggests that *in situ* pyrite formation is a slow process, underscoring the need for further studies to clarify the exact transformation sequence in natural settings.

The observed stability or transformation of Fe minerals in different biogeochemical conditions has important environmental implications. For instance, in sulfidic environments, the transformation of Fe-oxides to Fe–sulfide minerals reduces the phosphorus sorption capacity,[41] potentially increasing the release of bioavailable phosphorus and exacerbating coastal eutrophication. Conversely, trace elements like arsenic, which are strongly sorbed to Fe–sulfides, may become more immobilized,[80,81] altering the contaminant dynamics in coastal sediments. As coastal regions face increasing eutrophication and sulfate reduction driven by sea-level rise, understanding the transformation pathways and timescales of Fe minerals is crucial for predicting future biogeochemical changes in coastal sediments.

Conflicts of interest

There are no confllicts to declare.

Data availability

The data supporting this article have been included as part of the supplementary information (SI). Supplementary information: additional information on materials and methods, the characterization of the synthesized mineral phases and additional Mössbauer fits. Further, we present results of the transformation of pure mineral mesh-bags. See DOI: **https://doi.org/10.1039/d5em00213c**.

Acknowledgements

We thank Kurt Barmettler (ETH Zürich) and Andrew Grigg (ETH Zürich) for assisting with laboratory work. Field experiments

Open Access Article. Published on 18 2025. Downloaded on 14.05.2026 20:13:44.
This article is licensed under a Creative Commons Attribution 3.0 Unported Licence.

were conducted with permission from the National Park Administration, Landesbetrieb für Küstenschutz, Nationalpark and Meeresschutz Schleswig-Holstein, Germany. This work was funded by the European Research Council (ERC) under the European Union's Horizon 2020 research and innovation program (grant agreement no. 788009-IRMIDYN-ERC-2017-ADG).

References

1 D. E. Canfield, Reactive iron in marine sediments, *Geochim. Cosmochim. Acta*, 1989, **53**(3), 619–632.
2 S. Poulton and R. Raiswell, The low-temperature geochemical cycle of iron: from continental fluxes to marine sediment deposition, *Am. J. Sci.*, 2002, **302**(9), 774–805.
3 R. M. Cornell and U. Schwertmann, *et al.*, *The Iron Oxides: Structure, Properties, Reactions, Occurrences, and Uses*, Wiley-VCH, Weinheim, 2003, vol. 664.
4 F. A. Weber, A. Voegelin and R. Kretzschmar, Multi-metal contaminant dynamics in temporarily flooded soil under sulfate limitation, *Geochim. Cosmochim. Acta*, 2009, **73**(19), 5513–5527.
5 J. Middelburg and L. Levin, Coastal hypoxia and sediment biogeochemistry, *Biogeosciences*, 2009, **6**(7), 1273–1293.
6 C. M. Hansel, S. G. Benner and S. Fendorf, Competing Fe (II)-induced mineralization pathways of ferrihydrite, *Environ. Sci. Technol.*, 2005, **39**(18), 7147–7153.
7 D. D. Boland, R. N. Collins, C. J. Miller, C. J. Glover and T. D. Waite, Effect of solution and solid-phase conditions on the Fe (II)-accelerated transformation of ferrihydrite to lepidocrocite and goethite, *Environ. Sci. Technol.*, 2014, **48**(10), 5477–5485.
8 H. D. Pedersen, D. Postma, R. Jakobsen and O. Larsen, Fast transformation of iron oxyhydroxides by the catalytic action of aqueous Fe (II), *Geochim. Cosmochim. Acta*, 2005, **69**(16), 3967–3977.
9 R. W. Howarth and J. M. Teal, Sulfate reduction in a New England salt marsh 1, *Limnol. Oceanogr.*, 1979, **24**(6), 999–1013.
10 B. B. Jørgensen, Mineralization of organic matter in the sea bed— the role of sulphate reduction, *Nature*, 1982, **296**(5858), 643–645.
11 A. E. Giblin, Pyrite formation in marshes during early diagenesis, *Geomicrobiol. J.*, 1988, **6**(2), 77–97.
12 A. J. Pyzik and S. E. Sommer, Sedimentary iron monosulfides: Kinetics and mechanism of formation, *Geochim. Cosmochim. Acta*, 1981, **45**(5), 687–698.
13 S. W. Poulton, M. D. Krom and R. Raiswell, A revised scheme for the reactivity of iron (oxyhydr) oxide minerals towards dissolved sulfide, *Geochim. Cosmochim. Acta*, 2004, **68**(18), 3703–3715.
14 L. K. ThomasArrigo, C. Mikutta, R. Lohmayer, B. Planer-Friedrich and R. Kretzschmar, Sulfidization of organic freshwater flocs from a minerotrophic peatland: speciation changes of iron, sulfur, and arsenic, *Environ. Sci. Technol.*, 2016, **50**(7), 3607–3616.
15 C. M. Hansel, C. J. Lentini, Y. Tang, D. T. Johnston, S. D. Wankel and P. M. Jardine, Dominance of sulfur-fueled iron oxide reduction in low-sulfate freshwater sediments, *ISME J.*, 2015, **9**(11), 2400–2412.
16 B. B. Jørgensen, A. J. Findlay and A. Pellerin, The biogeochemical sulfur cycle of marine sediments, *Front. Microbiol.*, 2019, **10**, 436320.
17 K. Hellige, K. Pollok, P. Larese-Casanova, T. Behrends and S. Peiffer, Pathways of ferrous iron mineral formation upon sulfidation of lepidocrocite surfaces, *Geochim. Cosmochim. Acta*, 2012, **81**, 69–81.
18 S. Peiffer, T. Behrends, K. Hellige, P. Larese-Casanova, M. Wan and K. Pollok, Pyrite formation and mineral transformation pathways upon sulfidation of ferric hydroxides depend on mineral type and sulfide concentration, *Chem. Geol.*, 2015, **400**, 44–55.
19 M. Wan, C. Schröder and S. Peiffer, Fe (III): S (-II) concentration ratio controls the pathway and the kinetics of pyrite formation during sulfidation of ferric hydroxides, *Geochim. Cosmochim. Acta*, 2017, **217**, 334–348.
20 L. K. ThomasArrigo, S. Bouchet, R. Kaegi and R. Kretzschmar, Organic matter influences transformation products of ferrihydrite exposed to sulfide, *Environ. Sci.: Nano*, 2020, **7**(11), 3405–3418.
21 Q. Wang and J. W. Morse, Pyrite formation under conditions approximating those in anoxic sediments I. Pathway and morphology, *Mar. Chem.*, 1996, **52**(2), 99–121.
22 D. T. Rickard, Kinetics and mechanism of the sulfidation of goethite, *Am. J. Sci.*, 1974, **274**(8), 941–952.
23 M. Dos Santos Afonso and W. Stumm, Reductive dissolution of iron (III)(hydr) oxides by hydrogen sulfide, *Langmuir*, 1992, **8**(6), 1671–1675.
24 L. Notini, L. K. ThomasArrigo, R. Kaegi and R. Kretzschmar, Coexisting goethite promotes Fe (II)-catalyzed transformation of ferrihydrite to goethite, *Environ. Sci. Technol.*, 2022, **56**(17), 12723–12733.
25 C. Schröder, M. Wan, I. B. Butler, A. Tait, S. Peiffer and C. A. McCammon, Identification of mackinawite and constraints on its electronic configuration using Mössbauer spectroscopy, *Minerals*, 2020, **10**(12), 1090.
26 M. A. Schoonen, *Mechanisms of Sedimentary Pyrite Formation*, Special papers-Geological Society of America, 2004, pp. 117–134.
27 D. Rickard and G. W. Luther, Chemistry of iron sulfides, *Chem. Rev.*, 2007, **107**(2), 514–562.
28 R. Sweeney and I. Kaplan, Pyrite framboid formation; laboratory synthesis and marine sediments, *Econ. Geol.*, 1973, **68**(5), 618–634.
29 M. Schoonen and H. Barnes, Reactions forming pyrite and marcasite from solution: I. Nucleation of FeS_2 below 100° C, *Geochim. Cosmochim. Acta*, 1991, **55**(6), 1495–1504.
30 L. G. Benning, R. T. Wilkin and H. Barnes, Reaction pathways in the Fe–S system below 100°C, *Chem. Geol.*, 2000, **167**(1–2), 25–51.
31 A. Picard, A. Gartman, D. R. Clarke and P. R. Girguis, Sulfate-reducing bacteria influence the nucleation and growth of

 This journal is © The Royal Society of Chemistry 2025

Open Access Article. Published on 18 2025. Downloaded on 14.05.2026 20:13:44.
This article is licensed under a Creative Commons Attribution 3.0 Unported Licence.

mackinawite and greigite, *Geochim. Cosmochim. Acta*, 2018, **220**, 367–384.

32 J. Thiel, J. M. Byrne, A. Kappler, B. Schink and M. Pester, Pyrite formation from FeS and H_2S is mediated through microbial redox activity, *Proc. Natl. Acad. Sci. U. S. A.*, 2019, **116**(14), 6897–6902.

33 D. Rickard and G. W. Luther III, Kinetics of pyrite formation by the H_2S oxidation of iron (II) monosulfide in aqueous solutions between 25 and 125°C: The mechanism, *Geochim. Cosmochim. Acta*, 1997, **61**(1), 135–147.

34 J. Hua, J. Sun, M. Chen, C. Liu and F. Wu, Aqueous Fe (II)-catalyzed iron oxide recrystallization: Fe redox cycling and atom exchange, mineralogical recrystallization and contributing factor, *Rev. Environ. Sci. Bio/Technol.*, 2023, **22**(1), 55–78.

35 A. Thompson, O. A. Chadwick, D. G. Rancourt and J. Chorover, Iron-oxide crystallinity increases during soil redox oscillations, *Geochim. Cosmochim. Acta*, 2006, **70**(7), 1710–1727.

36 V. Vogelsang, S. Fiedler, R. Jahn and K. Kaiser, In-situ transformation of iron-bearing minerals in marshland-derived paddy subsoil, *Eurasian J. Soil Sci.*, 2016, **67**(5), 676–685.

37 P. Winkler, K. Kaiser, A. Thompson, K. Kalbitz, S. Fiedler and R. Jahn, Contrasting evolution of iron phase composition in soils exposed to redox fluctuations, *Geochim. Cosmochim. Acta*, 2018, **235**, 89–102.

38 M. Barczok, C. Smith, N. Di Domenico, L. Kinsman-Costello, D. Singer and E. Herndon, Influence of contrasting redox conditions on iron (oxyhydr) oxide transformation and associated phosphate sorption, *Biogeochemistry*, 2023, **166**(2), 87–107.

39 K. Schulz, L. Notini, A. R. Grigg, L. J. Kubeneck, W. Wisawapipat, L. K. ThomasArrigo, *et al.*, Contact with soil impacts ferrihydrite and lepidocrocite transformations during redox cycling in a paddy soil, *Environ. Sci.:Processes Impacts*, 2023, **25**(12), 1945–1961.

40 K. Schulz, W. Wisawapipat, K. Barmettler, A. R. Grigg, L. J. Kubeneck, L. Notini, *et al.*, Iron oxyhydroxide transformation in a flooded rice paddy field and the effect of adsorbed phosphate, *Environ. Sci. Technol.*, 2024, **58**(24), 10601–10610.

41 P. Kraal, C. M. van Genuchten, W. K. Lenstra and T. Behrends, Coprecipitation of phosphate and silicate affects environmental iron (oxyhydr) oxide transformations: A gel-based diffusive sampler approach, *Environ. Sci. Technol.*, 2020, **54**(19), 12795–12802.

42 L. J. Kubeneck, K. A. Rothwell, L. Notini, L. K. ThomasArrigo, K. Schulz, G. Fantappiè, *et al.*, In situ vivianite formation in intertidal sediments: Ferrihydrite-adsorbed P triggers vivianite formation, *Environ. Sci. Technol.*, 2025, **59**, 523–532.

43 L. J. Kubeneck, L. Notini, K. A. Rothwell, G. Fantappiè, T. Huthwelker, L. K. ThomasArrigo, *et al.*, Transformation of vivianite in intertidal sediments with contrasting sulfide conditions, *Geochim. Cosmochim. Acta*, 2024, **370**, 173–187.

44 P. Taylor, R. Maeck and P. De Bièvre, Determination of the absolute isotopic composition and atomic weight of a reference sample of natural iron, *Int. J. Mass Spectrom.*, 1992, **121**(1–2), 111–125.

45 A. R. Grigg, W. Wisawapipat, K. Barmettler, K. Schulz, L. Notini, L. K. ThomasArrigo, *et al.*, Stability and transformation of jarosite and Al-substituted jarosite in an acid sulfate paddy soil under laboratory and field conditions, *Geochim. Cosmochim. Acta*, 2024, **382**, 128–141.

46 J. D. Cline, Spectrophotometric determination of hydrogen sulfide in natural waters 1, *Limnol. Oceanogr.*, 1969, **14**(3), 454–458.

47 D. Rancourt and J. Ping, Voigt-based methods for arbitrary-shape static hyperfine parameter distributions in Mössbauer spectroscopy, *Nucl. Instrum. Methods Phys. Res.*, 1991, **58**(1), 85–97.

48 K. Lagarec and D. Rancourt, Extended Voigt-based analytic lineshape method for determining N-dimensional correlated hyperfine parameter distributions in Mössbauer spectroscopy, *Nucl. Instrum. Methods Phys. Res.*, 1997, **129**(2), 266–280.

49 T. J. Grundl, S. Haderlein, J. T. Nurmi and P. G. Tratnyek, Introduction to aquatic redox chemistry, in *Aquatic Redox Chemistry*, ACS Publications, Washington, DC, 2011, pp. 1–14.

50 K. B. Bartlett, D. S. Bartlett, R. C. Harriss and D. I. Sebacher, Methane emissions along a salt marsh salinity gradient, *Biogeochemistry*, 1987, **4**, 183–202.

51 R. J. Mortimer, A. M. Galsworthy, S. H. Bottrell, L. E. Wilmot and R. J. Newton, Experimental evidence for rapid biotic and abiotic reduction of Fe (III) at low temperatures in salt marsh sediments: a possible mechanism for formation of modern sedimentary siderite concretions, *Sedimentology*, 2011, **58**(6), 1514–1529.

52 C. Chen and A. Thompson, The influence of native soil organic matter and minerals on ferrous iron oxidation, *Geochim. Cosmochim. Acta*, 2021, **292**, 254–270.

53 L. Notini, K. Schulz, L. J. Kubeneck, A. R. Grigg, K. A. Rothwell, G. Fantappiè, *et al.*, A new approach for investigating iron mineral transformations in soils and sediments using ^{57}Fe-labeled minerals and ^{57}Fe Mössbauer spectroscopy, *Environ. Sci. Technol.*, 2023, **57**(27), 10008–10018.

54 K. Eusterhues, F. E. Wagner, W. Häusler, M. Hanzlik, H. Knicker, K. U. Totsche, *et al.*, Characterization of ferrihydrite-soil organic matter coprecipitates by X-ray diffraction and Mossbauer spectroscopy, *Environ. Sci. Technol.*, 2008, **42**(21), 7891–7897.

55 N. Blaes, H. Fischer and U. Gonser, Analytical expression for the Mössbauer line shape of ^{57}Fe in the presence of mixed hyperfine interactions, *Nucl. Instrum. Methods Phys. Res.*, 1985, **9**(2), 201–208.

56 M. Aeppli, R. Kaegi, R. Kretzschmar, A. Voegelin, T. B. Hofstetter and M. Sander, Electrochemical analysis of changes in iron oxide reducibility during abiotic ferrihydrite transformation into goethite and magnetite, *Environ. Sci. Technol.*, 2019, **53**(7), 3568–3578.

57 K. Schulz, L. K. ThomasArrigo, R. Kaegi and R. Kretzschmar, Stabilization of ferrihydrite and lepidocrocite by silicate

Open Access Article. Published on 18 2025. Downloaded on 14.05.2026 20:13:44.
This article is licensed under a Creative Commons Attribution 3.0 Unported Licence.

during Fe (II)-catalyzed mineral transformation: Impact on particle morphology and silicate distribution, *Environ. Sci. Technol.*, 2022, **56**(9), 5929–5938.

58 U. Schwertmann and R. Taylor, The influence of silicate on the transformation of lepidocrocite to goethite, *Clay Miner.*, 1972, **20**, 159–164.

59 C. Liu, Z. Zhu, F. Li, T. Liu, C. Liao, J. J. Lee, *et al.*, Fe (II)-induced phase transformation of ferrihydrite: The inhibition effects and stabilization of divalent metal cations, *Chem. Geol.*, 2016, **444**, 110–119.

60 J. Chi, Y. Ou, F. Li, W. Zhang, H. Zhai, T. Liu, *et al.*, Cooperative roles of phosphate and dissolved organic matter in inhibiting ferrihydrite transformation and their distinct fates, *Sci. Total Environ.*, 2024, **908**, 168376.

61 E. J. O'Loughlin, C. A. Gorski, M. M. Scherer, M. I. Boyanov and K. M. Kemner, Effects of oxyanions, natural organic matter, and bacterial cell numbers on the bioreduction of lepidocrocite (γ-FeOOH) and the formation of secondary mineralization products, *Environ. Sci. Technol.*, 2010, **44**(12), 4570–4576.

62 Q. Wang, J. Wang, X. Wang, N. Kumar, Z. Pan, S. Peiffer, *et al.*, Transformations of ferrihydrite–extracellular polymeric substance coprecipitates driven by dissolved sulfide: interrelated effects of carbon and sulfur loadings, *Environ. Sci. Technol.*, 2023, **57**(10), 4342–4353.

63 R. M. Handler, B. L. Beard, C. M. Johnson and M. M. Scherer, Atom exchange between aqueous Fe (II) and goethite: An Fe isotope tracer study, *Environ. Sci. Technol.*, 2009, **43**(4), 1102–1107.

64 D. E. Latta, J. E. Bachman and M. M. Scherer, Fe electron transfer and atom exchange in goethite: Influence of Al-substitution and anion sorption, *Environ. Sci. Technol.*, 2012, **46**(19), 10614–10623.

65 C. van der Zee, D. R. Roberts, D. G. Rancourt and C. P. Slomp, Nanogoethite is the dominant reactive oxyhydroxide phase in lake and marine sediments, *Geology*, 2003, **31**(11), 993–996.

66 M. Spender, J. Coey and A. Morrish, The magnetic properties and Mössbauer spectra of synthetic samples of Fe_3S_4, *Can. J. Phys.*, 1972, **50**(19), 2313–2326.

67 R. Vandenberghe, E. De Grave, P. De Bakker, M. Krs and J. Hus, Mössbauer effect study of natural greigite, *Hyperfine Interact.*, 1992, **68**, 319–322.

68 S. Hunger and L. G. Benning, Greigite: a true intermediate on the polysulfide pathway to pyrite, *Geochem. Trans.*, 2007, **8**, 1–20.

69 G. W. Luther III, A. Giblin, R. W. Howarth and R. A. Ryans, Pyrite and oxidized iron mineral phases formed from pyrite oxidation in salt marsh and estuarine sediments, *Geochim. Cosmochim. Acta*, 1982, **46**(12), 2665–2669.

70 R. W. Howarth, Pyrite: its rapid formation in a salt marsh and its importance in ecosystem metabolism, *Science*, 1979, **203**(4375), 49–51.

71 N. Harmandas, E. Navarro Fernandez and P. Koutsoukos, Crystal growth of pyrite in aqueous solutions. Inhibition by organophosphorus compounds, *Langmuir*, 1998, **14**(5), 1250–1255.

72 G. W. Luther III, Pyrite synthesis via polysulfide compounds, *Geochim. Cosmochim. Acta*, 1991, **55**(10), 2839–2849.

73 H. Y. Jeong, Y. S. Han, S. W. Park and K. F. Hayes, Aerobic oxidation of mackinawite (FeS) and its environmental implication for arsenic mobilization, *Geochim. Cosmochim. Acta*, 2010, **74**(11), 3182–3198.

74 D. Cheng, S. Yuan, P. Liao and P. Zhang, Oxidizing impact induced by mackinawite (FeS) nanoparticles at oxic conditions due to production of hydroxyl radicals, *Environ. Sci. Technol.*, 2016, **50**(21), 11646–11653.

75 H. Ma, P. Wang, A. Thompson, Q. Xie, M. Zhu, H. H. Teng, *et al.*, Secondary mineral formation and carbon dynamics during FeS oxidation in the presence of dissolved organic matter, *Environ. Sci. Technol.*, 2022, **56**(19), 14120–14132.

76 M. Ma, P. Overvest, A. Hijlkema, S. Mangold, C. McCammon, A. Voegelin, *et al.*, Phosphate burial in aquatic sediments: Rates and mechanisms of vivianite formation from mackinawite, *Chem. Eng. J. Adv.*, 2023, **16**, 100565.

77 M. Etique, S. Bouchet, J. M. Byrne, L. K. ThomasArrigo, R. Kaegi and R. Kretzschmar, Mercury reduction by nanoparticulate vivianite, *Environ. Sci. Technol.*, 2021, **55**(5), 3399–3407.

78 S. Peiffer, A. Kappler, S. Haderlein, C. Schmidt, J. Byrne, S. Kleindienst, *et al.*, A biogeochemical–hydrological framework for the role of redox-active compounds in aquatic systems, *Nat. Geosci.*, 2021, **14**(5), 264–272.

79 G. Zhao, M. Tan, B. Wu, X. Zheng, R. Xiong, B. Chen, *et al.*, Redox oscillations activate thermodynamically stable iron minerals for enhanced reactive oxygen species production, *Environ. Sci. Technol.*, 2023, **57**(23), 8628–8637.

80 M. Wolthers, L. Charlet, C. H. van Der Weijden, P. R. Van der Linde and D. Rickard, Arsenic mobility in the ambient sulfidic environment: Sorption of arsenic (V) and arsenic (III) onto disordered mackinawite, *Geochim. Cosmochim. Acta*, 2005, **69**(14), 3483–3492.

81 N. K. Niazi and E. D. Burton, Arsenic sorption to nanoparticulate mackinawite (FeS): an examination of phosphate competition, *Environ. Pollut.*, 2016, **218**, 111–117.

 This journal is © The Royal Society of Chemistry 2025